JOURNAL OF MATERIALS SCIENCE 31 (1996) 2009–2017

Synthesis and microstructure of nanostructured $Al/Al_2O_3(H)$-composite

M. VEITH, S. FABER
Anorganische Chemie, Universität des Saarlandes, D-66123 Saarbrücken, Germany
R. HEMPELMANN, S. JANSSEN*, J. PREWO
Physikalische Chemie, Universität des Saarlandes, D-66123 Saarbrücken, Germany
H. ECKERLEBE
GKSS Forschungszentrum, D-21502 Geesthacht, Germany

By means of a metal organic chemical vapour deposition, starting from a single precursor compound $[tBuOAlH_2]_2$, an aluminium/aluminium hydrido-oxide composite has been synthesized in thin layers. Electron micrographs indicate self-similarity. A detailed analysis by small angle neutron scattering directly yields a surface fractal microstructure with a fractal dimension of 2.26; in the framework of a surface fractal model we determine the relevant particle dimensions and their size distribution.

1. Introduction

The synthesis of materials which combine at the same time a metallic and a ceramic phase (for example a metal/metal oxide composite) may be performed by different means. Solid state reactions between the components may be achieved when the different phases are brought into intimate contact in a ball mill or by other powder metallurgical processes [1, 2]. Further techniques use the infiltration of one component into the other by liquid–solid or gas–solid processes [3, 4]. Also by using the redox reaction between a metal and an oxide, in special cases metal/metal oxide composites have been formed (see for example the DIMOX™-process) [5, 6]. All procedures discussed so far use the interaction of at least two components. The components may be present in chemical pure form (for example aluminium and aluminium oxide) and thus only have to be mixed up.

On the other hand, the components may also be formed in a chemical reaction and combined during the process, e.g. as in metal-organic chemical vapour deposition (MOCVD). In this chemical process several molecules (precursors) are brought together which contain the elements of the desired solid in well defined fractions. In the reactor the molecules undergo transformations yielding a solid which may be deposited as a layer, a powder or as a surface coating on a complicated tool or an integrated electronic circuit [7, 8].

There are few cases known where only "one" precursor is used in a MOCVD process instead of several and in which a "composite system" of "different phases" is formed. We have recently used a mixed metal alkoxide, $BaSn_2(OtBu)_6$, as precursor, and have characterized (after thermolysis) a composite which contains equal amounts of tin and barium stannate, $BaSnO_3$ [9]. Thus in this process a redox reaction is taking place within the precursor $BaSn_2(OtBu)_6$ forming two different tin species (tin (0) and tin (IV)) in two different phases.

Here we report a similar experiment starting with a single compound, $[tBuOAlH_2]_2$, which during the decomposition forms metallic aluminium together with an aluminium hydrido-oxide. We could imagine that in the future these new approaches of composite synthesis via MOCVD in "one component systems" may become as important as the formation of metal surfaces by gas techniques [10]. The microstructure of the resulting composite, characterized by small angle neutron scattering, corresponds to a surface fractal.

2. Experimental procedure

The synthesis has been performed under dry nitrogen (helium) gas using Schlenck techniques. NMR spectra have been measured on a Bruker-200 MHz AC 200p (liquids) or a 200 MHz-MSL 200 (solids) with magic angle spinning (MAS). Electron microscopy and the energy dispersive X-ray (EDX) analyses were performed on a scanning electron microscope CAMSCAN S4 with Si(Li)-semiconductor detectors and with thin windows (Cameca and Noran). For the X-ray powder diffraction Debye–Scherrer cameras of the Philips company and for the light microscopy a BX 60 apparatus of Olympus have been used. Infrared spectra were recorded on the model 883 of the Perkin Elmer company while the gas analysis has been performed with a quadrupole mass spectrometer QMG 125 of Balzer.

*Also at: Labor für Neutronenstreuung, Paul-Scherrer-Institut, CH-5232 Villigen-PSI.

0022–2461

The small angle neutron scattering experiment has been performed at the GKSS research centre at Geesthacht, Germany. An incident wavelength of $\lambda = 0.53$ nm with a wavelength spread of $\Delta\lambda/\lambda \approx 10\%$ was used at detector distances and respective collimations of 1, 4 and 17 m. The aluminium/aluminium hydrido-oxide sample was deposited on a 1 mm quartz plate. The sample thickness itself was 360 μm. Correspondingly, the transmission turned out to be very large, i.e. $T = 0.98$; therefore multiple scattering effects can be excluded. The scattering intensities were transformed into absolute units, $d\Sigma/d\Omega$, with a vanadium standard. All data were taken at room temperature.

3. Synthesis and chemical characterization

3.1. Synthesis of the precursor $(tBuOAlH_2)_2$

Following established routes [11] 4.554 g (120 mmol) $LiAlH_4$ are dissolved in 80 ml diethyl ether in a flask with a reflux cooler. Under cooling 5.334 g (40 mmol) of aluminium trichloride are dissolved in 80 ml diethyl ether and added to the lithium aluminium hydride in a steady flow at room temperature. Lithium chloride precipitates from the mixture. To this suspension 11.859 g (160 mmol) tert-butanole is added dropwise and formation of hydrogen is observed. The procedure is finished by a 4–5 h stirring at ambient temperature. After separation of the lithium chloride by filtration the solvent is evaporated *in vacuo*. The remaining solid is sublimated at ambient temperature and 100 Pa pressure thus obtaining 15.2 g bis(tert-butoxy aluminium dihydride) (93% yield) $(C_4H_9OAlH_2)_2$, calculated molecular mass 204.22 g mol^{-1}, determined by cryoscopy in benzene: 185 g mol^{-1}, ^{1}H NMR (δ, i-TMS): 1.22 p.p.m. (s, 18H, $-C(CH_3)_3$, 4.43 p.p.m. (s, $-AlH_2$); ^{13}C NMR (δ, i–TMS); 30.36 p.p.m. ($-CH_3$), 76.43 p.p.m. ($-C(CH_3)_3$), IR (hexane solution): 1846 cm^{-1} (νAlH_2); analytical data: 47.02 wt % C (calc. 47.00%), 10.65% H (calc. 10.86%).

3.2. Synthesis of the precursor $(tBuOAlD_2)_2$

The synthesis of $(tBuOAlD_2)_2$ is similar to that of $(tBuOAlH_2)_2$, but instead of $LiAlH_4$, $LiAlD_4$ is used. In the NMR spectrum one signal is found at 1.22 p.p.m. while the signal at 4.43 p.p.m. (hydride) has vanished. The $\nu(D_2Al)$ band is found at 1347 cm^{-1} in the infrared spectrum, roughly a factor $2^{-1/2}$ lower than the corresponding hydrogen vibration.

3.3. MOCVD process

The thermolysis of $(tBuO)AlH_2$ is performed in an apparatus similar to the one we have used with $BaSn_2(OtBu)_6$ [9]. The reaction is achieved by inductive heating of a graphite block in which a small sheet of quartz is inserted (see Fig. 1) and which is exposed to a steady stream of the precursor at an average pressure of 100 Pa. The precursor decomposes within the graphite block, and deposition of solid material takes place on the graphite as well as on the quartz surface. As quartz is a very bad thermal conductor the deposition on the surface can be considered as a cold trap region within the graphite block. No contamination of the formed layer by organic molecules is observed as the system is dynamic, with all volatile particles being trapped by liquid nitrogen. The volatile material can be analysed in a quadrupole mass spectrometer which is coupled to the apparatus by a valve.

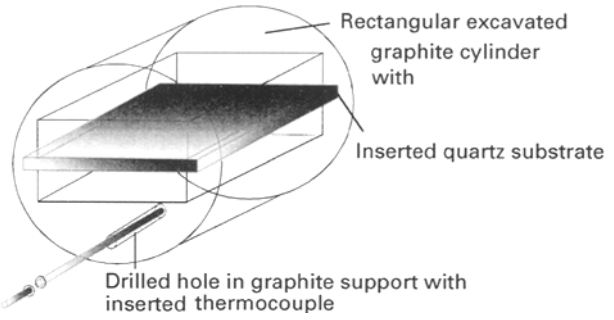

Figure 1 Graphite support with a quartz sheet inserted into the block.

In a typical experiment we have used 0.5 g $[AlH_2(OtBu)]_2$, 300–320 °C at the graphite block and 100 Pa pressure. Depending on the time of exposure layers of a grey material have been deposited on the quartz surface with a thickness of 20 nm to 1 mm. X-ray diffraction of the composite at room temperature reveals elemental aluminium to be the only crystalline phase. The corresponding diffraction peaks exhibit hardly any broadening. Heating of the sample to 600° C for several hours transforms part of the amorphous phase to γ-Al_2O_3 as found from X-ray powder diffraction [12]. Iso-butene and hydrogen can be detected as volatile decomposition products during the process by the mass spectrometer coupled to the thermolysis apparatus.

We have repeated the decomposition with the deuterated aluminium tert-butoxyhydride $[Al(OtBu)D_2]_2$ as described above. In the gas spectrum, apart from iso-butene, HD is detected as the major product.

Electron microscopy has been used to specify the solid compound. EDX analyses reveal approximately 1:1 correspondence of Al to oxygen (Standard-probe Al_2O_3) as in the precursor. Elemental analyses give the following proportions: 0.85 wt % H, 0.38% C, 62.4% Al which is in accord with the formula of approximate stoichiometry $H_{1.11}Al_{3.04}O_{3.00}$. ^{27}Al solid-state NMR spectroscopy using MAS shows two resonances, a broad band at 36 p.p.m. and a sharp peak at 1640 p.p.m. which is accompanied by spinning side bands. The ^{1}H NMR (MAS) spectrum of $[H_2AlOtBu]_2$ consists of two signals at 4.2 and 0.7 p.p.m.

3.4. Discussion of the chemical composition

The synthesis of the precursors have been performed according to:

$$AlCl_3 + 3LiAlH_4 \rightarrow 4\{AlH_3\} + 3LiCl \quad (1)$$

$$2\{AlH_3\} + 2tBuOH \rightarrow [H_2AlOtBu]_2 + 2H_2 \quad (2)$$

replacing H by D(^{2}H) yields:

$$[D_2AlOtBu]_2$$

2

The dimeric structure of **1** and **2** may be deduced from molar mass determination in solution (benzene). The compounds form solids which are easily volatile (see experimental section).

The mass spectroscopic control of the decomposition reaction of **1** or **2** reveals in both cases iso-butene as the organic decomposition fragment. The other volatile gas is the hydrogen molecule. In the mass spectrum of **2**, HD is about ten times more abundant than D_2, no deuterated iso-butene is found in this spectrum. From this finding, it is evident that one part of the produced hydrogen molecule must originate from the hydrogen attached to aluminium while the other hydrogen atoms originate from the former tert-butoxy group. From the decomposition reaction, the following Equation 3 can be proposed which is consistent with the gas phase analysis:

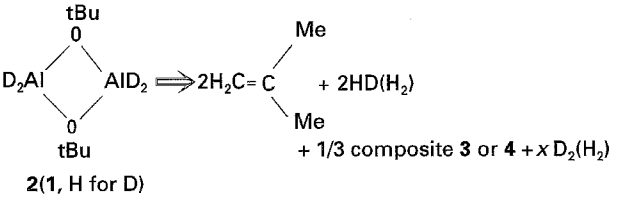

(3)

approximate composition of composite **3**:

$$2\ Al \cdot Al_2O_3 \cdot Al_2O_{3-n}H_{2n}\ (n \approx 1)$$

composite **4**:

$$2\ Al \cdot Al_2O_3 \cdot Al_2O_{3-n}D_{2n}\ (n \approx 1)$$

Composite **3** or **4** forms a grey material. The carbon content is, according to the elemental analysis, around 0.4% and can be neglected as a major component (surface absorption of organic gases). From the aluminium and hydrogen analysis, the approximate formula $H_{1.11}Al_{3.04}O_{3.00}$ can be deduced which corresponds to an atomic hydrogen fraction of 15.5%. X-ray diffraction on the powder reveals crystalline aluminium as one component of the composite. The oxide (hydride) does not show up in the diffraction pattern and seems to be amorphous. Heating the sample to 600° C under dry nitrogen leads to the formation of γ-Al_2O_3. The aluminium oxide as well as the metallic aluminium components are also detected in ^{27}Al NMR (see Fig. 2) in two distinct regions of the spectrum. While the resonance for the Al^{3+} is broad, suggesting different bonding types, the elemental aluminium is easily recognized by its spinning side bands and the typical Knight-shift [13]. Hydrogen is identified in the ^{1}H NMR MAS spectrum of composite **3** with a broad resonance centred at 4.5 p.p.m., typical for Al–H bond as in the precursor. Besides this peak **3** gives another sharp resonance at 0.7 p.p.m. The origin of this resonance is not quite clear; it may tentatively be assigned to organic residues which are sticking on the surface of

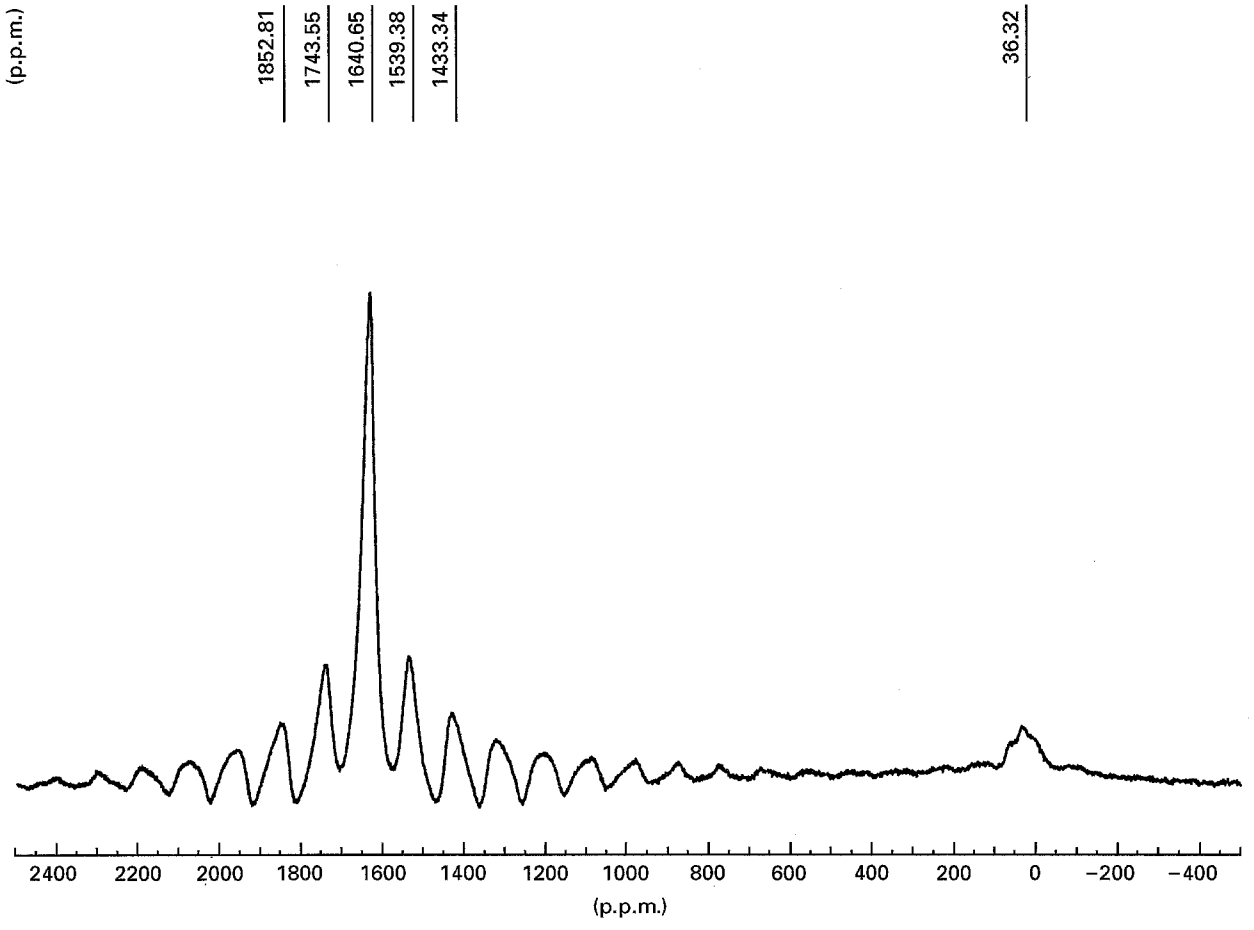

Figure 2 ^{27}Al NMR (MAS) of the solid composite.

the composite. Further investigations have to be done to clarify this point. A diffuse reflectance IR spectrum of powdered $Al/Al_2O_3(H)$-composite in KBr shows a broad absorption band for ν(AlH) at 1930 cm^{-1} in accordance with the findings of the NMR experiments (see above). EDX analysis of the solid is consistent with a one-to-one ratio of aluminium to oxygen in **3** in accord with the elemental analysis.

Taking all facts into consideration we have produced a nanocomposite by single precursor MOCVD techniques, which is made up of metallic aluminium as well as an amorphous matrix which has Al–O and Al–H bonds. There is an interesting relationship to the composite material we have obtained from $BaSn_2(OtBu)_6$: this one also consists of spheres which contain metallic tin besides $BaSnO_3$ [9].

4. Electron and optical microscopy

The microstructure of the composite material which has been obtained from **3** has been studied by means of electron and optical microscopy. On the graphite the deposited solid shows a coherent surface on which half-spheres can easily be recognized (Fig. 3). The whole compound seems to consist of interpenetrating spheres. These spheres grow into three-dimensional assemblies on inspection of the quartz surface (Fig. 4). As can easily be recognized each sphere is made up of smaller spheres which again seem to be generated by an assembly of balls. In an alternative experiment we have been able to show that the surfaces are generated from globular structures. When a thin quartz surface is exposed for a short period of time to precursor **1** in the MOCVD apparatus, a scanning electron microscopy (SEM) picture can be obtained which shows exclusively ball shaped components sticking onto the quartz surface (Fig. 5). Using transmission electron microscopy (TEM), we have again detected globular species of about 400 nm diameter which have spherical particles of 40 nm on their surface (Fig. 6). Again using TEM, we have been able to recognize aluminium crystals obtained from the composite by mechanical destruction (the crystals have diameters ranging from 5 to 140 nm, Fig. 7). The results on the microstructure obtained by microscopic techniques will be discussed later in connection with the small angle neutron scattering results to be presented in the next section.

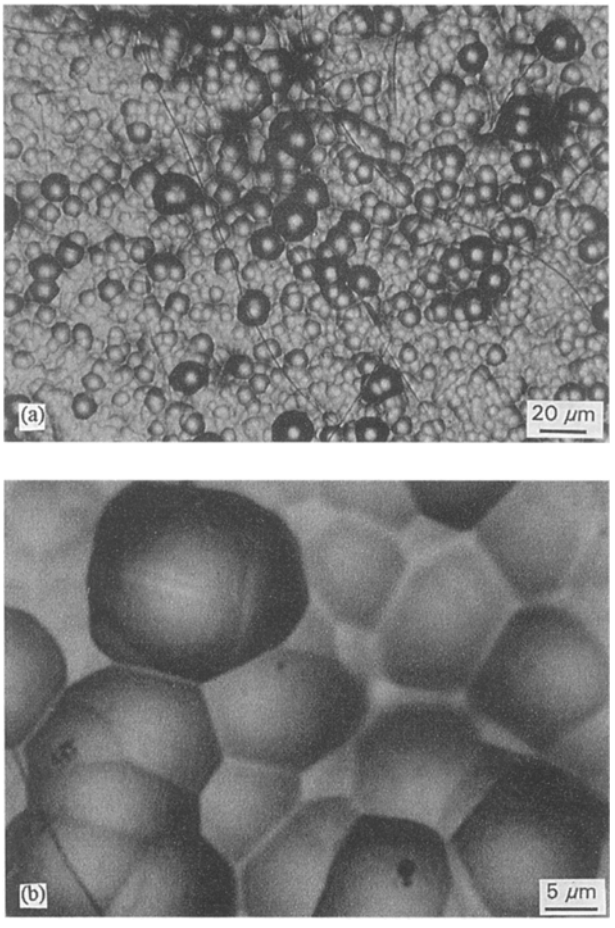

Figure 3 Half-spheres of the composite material deposited on graphite (light microscopy).

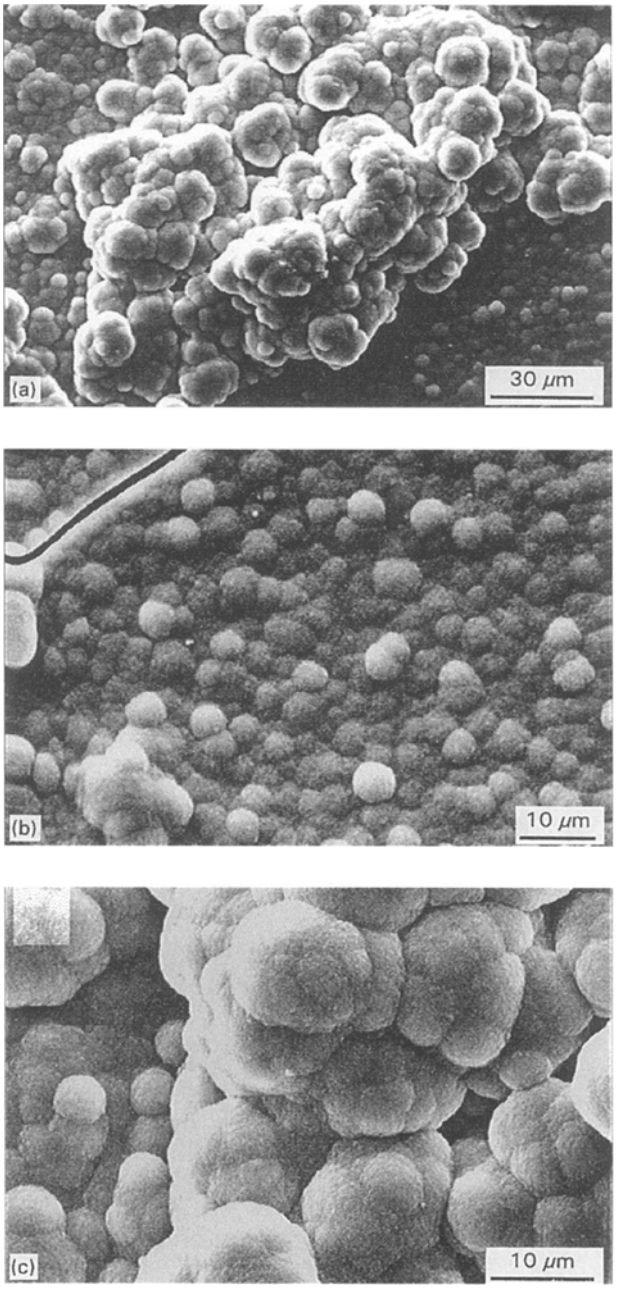

Figure 4 Scanning electron microscope pictures of the composite deposited on quartz.

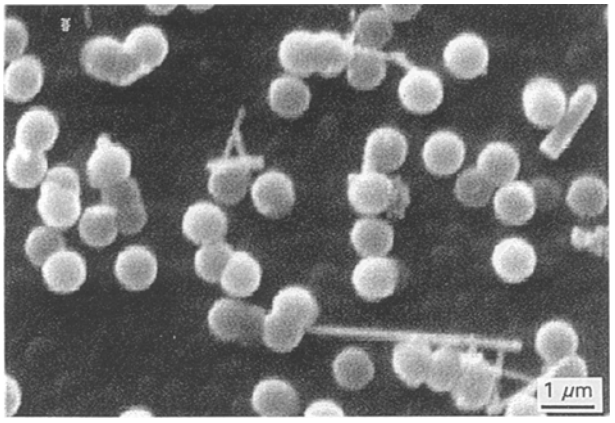

Figure 5 Ball-shaped particles of the composite sticking on a quartz substrate (SEM).

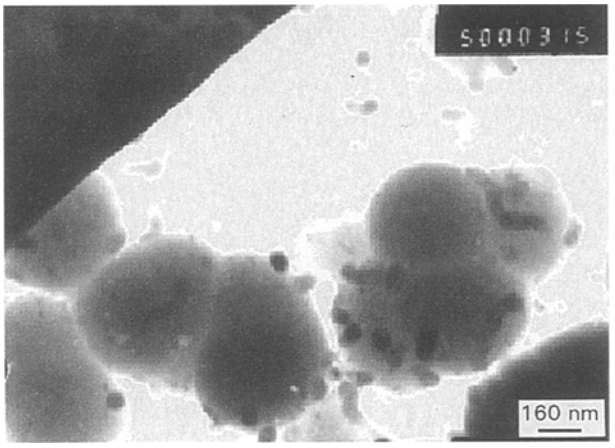

Figure 6 TEM of particles of the composite.

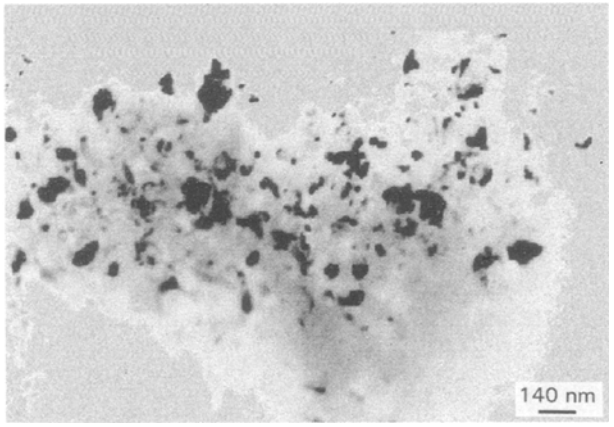

Figure 7 TEM picture of the ground composite. The aluminium crystals can be detected as black spots.

5. Small angle neutron scattering

Neutrons in non-magnetic matter are scattered by the different nuclei of the sample according to their respective scattering lengths b. In the case of coherent neutron scattering the neutron waves emanating from the different scattering centres interfere, i.e. the scattering amplitudes add up with their respective phase factor. In the case of incoherent neutron scattering, interference is not possible and the measured intensity is the sum of the individual scattering intensities. Other than the (common) wide angle scattering techniques small angle neutron scattering (SANS) is not able to "see" individual atoms, but the scattering signal arises from large-scaled inhomogeneities with characteristic lengths between 1 and 100 nm. Therefore SANS can be used to probe the structure of matter at a mesoscopic scale (between the atomistic and the macroscopic scale) which is often called the microstructure of the material and which is essential for the macroscopic properties.

5.1. Theoretical background

The differential cross-section obtained from the scattering intensity of a SANS experiment is given by

$$\frac{d\Sigma}{d\Omega}(Q) = \left| \int_{-\infty}^{+\infty} \rho(\mathbf{r}) \exp(i\mathbf{Q}\mathbf{r})\, d^3\mathbf{r} \right|^2 + \left(\frac{d\Sigma}{d\Omega}\right)_{inc} \quad (4)$$

with the scattering length density $\rho(\mathbf{r}) = \Sigma b_i N_i/V$ and the scattering vector $\mathbf{Q}$, the absolute value of which is related to the scattering angle ϑ by $Q = (4\pi/\lambda)\sin(\vartheta/2)$ for elastic scattering. $\hbar Q$ is called the momentum transfer. The second term in Equation 4 denotes the incoherent contribution to the cross-section that arises from deviations of the scattering length density from its average value. The incoherent scattering is Q-independent and thus provides no information about the structure. The incoherent differential cross-section is given by

$$\left(\frac{d\Sigma}{d\Omega}\right)_{inc} = \frac{1}{4\pi} \sum_i \frac{N_i}{V} \sigma_i^{inc} \quad (5)$$

with the particle number densities N_i/V and the incoherent neutron scattering cross-sections σ_i^{inc}. For the composite material the main contribution to the incoherent cross-section arises from hydrogen within the sample, because σ^{inc} for Al and for O is negligible compared to the value for H.

The integrated differential cross-section is called the invariant J due to its independence of structural details of the sample. J is related to the difference in scattering length density, the so called scattering contrast $\Delta\rho$, and to the volume fraction of scattering particles υ_c by the Equation [14]

$$J = \int_0^\infty \frac{d\Sigma}{d\Omega}(Q)\, Q^2\, dQ = 2\pi^2(\Delta\rho)^2\, \upsilon_c(1 - \upsilon_c) \quad (6)$$

Thus by knowing the scattering contrast υ_c can be evaluated from J. As will be shown below, the scattering contrast in our composite is mainly due to pores.

Fractals [15] are characterized by their self-similarity within a certain variation in length scale. The mass scales with the linear dimension r as $m(r) \propto r^D$ where D is the so-called fractal dimension. Fractals as models of microstructure play an important role in the theoretical description of porous matter. Pore spaces and pore interfaces of rocks [16, 17] and of brown coal [18] have been treated with this approach. For a random distribution of shapes and sizes of non-interacting pores the small angle scattering was

evaluated by Porod [19, 20] and Debye *et al.* [21] yielding the so called "Porod law"

$$\frac{d\Sigma}{d\Omega}(Q) \propto Q^{-4} \tag{7}$$

provided that the surfaces of the pores are smooth; this Q^{-4} dependence is plausible for the single particle form factor of monodisperse spheres (see Equation 9 below) which exhibits a modulated Q^{-4} behaviour in the limit of large momentum transfer ($Q \gg \{\text{average pore radius}\}^{-1}$) provided that the small Q approximation Equation 4 remains valid; with some polydispersity the modulation vanishes. Bale and Schmidt [18] extended the derivation of scattering on inner surfaces to randomly distributed fractal surfaces and found

$$\frac{d\Sigma}{d\Omega}(Q) \propto Q^{-(6-D_s)} \tag{8}$$

where $2 \leqslant D_s \leqslant 3$ is the fractal dimension of the surface. For $D_s = 2$ (smooth surface) the Porod law is recovered. The microstructure considered above corresponds to comparatively bulk matter with some pores of different sizes. However, there exists comparatively loose porous materials, for instance aerogels or polymer networks, which do not exhibit well defined surfaces; in the case of self-similarity, this type of microstructure is called volume fractal. Small angle scattering on volume fractals yields [22, 23]

$$\frac{d\Sigma}{d\Omega}(Q) \propto Q^{-D_v} \tag{9}$$

where $D_v \leqslant 3$ is the fractal dimension of the structure. Thus, in a SANS experiment, a power law extending over several orders of magnitude in Q indicates fractal behaviour [24], and according to Equations 8 and 9 the distinction between surface and volume fractals is straightforward.

Schmidt and Tang have developed a model of a non-random surface fractal, which provides the first exact solution for the small angle scattering from such a structure (see [24] and references therein). The model consists of a collection of spheres as shown in Fig. 8. The central one with radius a_0, being located in the origin of a Cartesian coordinate system, is surrounded by six spheres of radius a_0/b on the positive and negative coordinate axes. b denotes the scaling factor between the radii of two successive generations of spheres and is related to the fractal dimension D_s by $D_s = \log 5/\log b$. The subsequent iterations are obtained by surrounding every sphere by five spheres of radius a_0/b^n in the directions parallel to the coordinate axes except the direction back to the generating sphere. For such a model the authors obtain the following scattering law:

$$\frac{d\Sigma}{d\Omega}(Qa_0) = (\Delta\rho V_0)^2 \{K_n(Qa_0) + L_n(Qa_0)\} \tag{10}$$

with $V_0 = (4\pi/3)a_0^3$. The first term in Equation 10 denotes the contribution that is obtained from an ensemble of independently scattering spheres. K_n

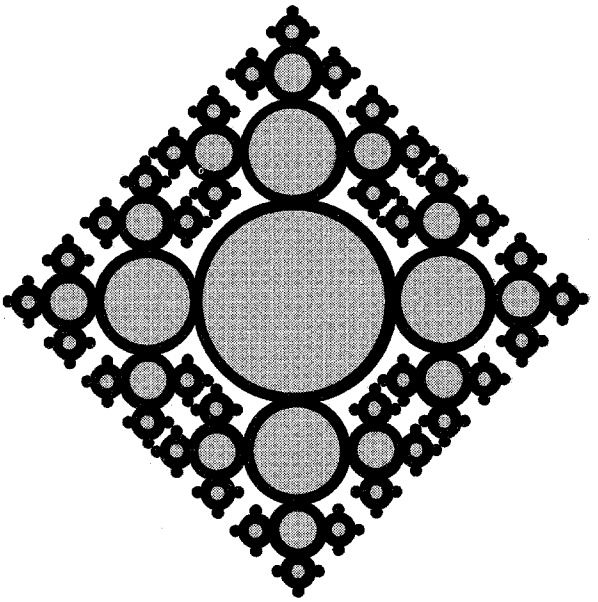

Figure 8 Surface fractal model: the central sphere of radius a_0 is surrounded by six spheres of radius $a_1 = a_0/b$, and so on.

is given by

$$K_n(Qa_0) = \frac{6}{5}\sum_{i=0}^{n}\left\{\left(\frac{5}{b^6}\right)^i\left[F\left(Q\frac{a_0}{b^i}\right)\right]^2 - \frac{1}{5}[F(Qa_0)]^2\right\} \tag{11}$$

with

$$F(y) = 3[(\sin y - y\cos y)/y^3)] \tag{12}$$

where $F^2(Qa_0)$ represents the form factor of spheres with radius a_0. From the micrographs (Section 4) we know that our system is composed of spherical particles. Each sphere consists of a kernel of elemental Al surrounded by a shell of Al_2O_3. The volume fraction of the kernel Al, is large for large spheres but small for small spheres. In other words, there does not exist a fixed ratio (coherence) between the radii of kernel and sphere. Therefore the scattering from kernel and shell cannot interfere, and in our fractal model we keep on considering the particles as spheres but with an averaged scattering length density. The second term in Equation 10, L_n, arises from interference effects of the different spheres. Therefore L_n depends on all the distances r_{ij} between the different spheres. According to Schmidt [24], by taking into account the effect of polydispersity, i.e. the presence of a distribution function for the radius of the central sphere a_0, the interference term becomes negligible, and thus the only noticeable contribution arises from the term K_n. For the distribution function in the evaluation of our SANS data, we have used the exponential distribution function

$$\varphi_m(a_0) = \frac{1}{R\Gamma(m+1)}(a_0/R)^m \exp(-a_0/R) \tag{13}$$

with the gamma function $\Gamma(z) = \int_0^\infty t^{z-1}e^{-t}\,dt$ as the normalization constant. The parameters R and m characterize the slope of the leading and the trailing edges of the distribution function, respectively (see

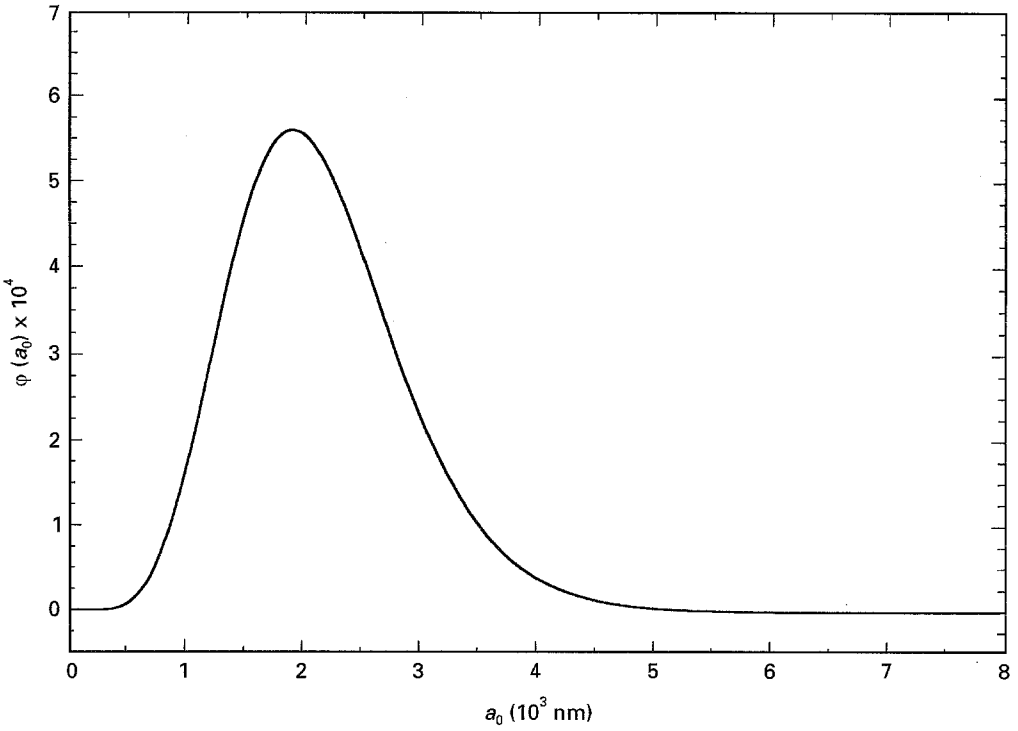

Figure 9 Normalized size distribution function $\varphi_m(a_0)$ for the radius a_0 of the central sphere. A maximum is obtained at about $a_0 = 2000$ nm.

Fig. 9 later on). An exponential distribution function is commonly used for molar masses of polymers (see e.g. [25]) and was also applied by Schmidt [24]. The essential feature of such a distribution, see Fig. 9, consists in its asymmetry: there are, as in reality, no particles (molecules) with zero radius (molar mass), whereas particles with a radius several times larger than the most likely value do occur, with low but finite probability. The quantity K_n in Equation 7 is then replaced by

$$K_{nm}(Qa_0) = \int_0^\infty \varphi_m(a_0) K_n((Qa_0)\, da_0 \qquad (14)$$

In this way we model our system as an ensemble of independently scattering surface fractals consisting of spheres. The self-similarity is included in the scale factor b. The data evaluation yields information about the fractal dimension, the shape of the distribution function and the size of the spheres.

5.2. Results

Fig. 10 presents the experimental results for the differential cross-section $d\Sigma/d\Omega$ as a function of the momentum transfer Q. The incoherent background dominates at values of $Q > 0.8\ nm^{-1}$. The data were collected over almost five orders of magnitude in intensity and roughly two orders of magnitude in Q. The data imply three detector distances (1, 4, and 17 m); the shortest detector distance covers mostly values of Q where the coherent cross-section decreased below the incoherent background level.

Within the error bars a tiny systematic deviation between the experimental data points and the solid line can be noticed. A change of curvature occurs at the value of Q where the two detector distances show up their overlap. This might be an artefact due to the detector channel efficiency. Here a correction is almost impossible because the efficiency not only varies with the detector channel but also with the increasing intensity leading to different characteristics in the two data sets collected at different scattering count rates.

5.2.1. Model-independent data evaluation

From the double logarithmic representation in Fig. 10 a power law in Q (see Equations 7 and 8) with an exponent of $\alpha = 3.74 \pm 0.05$ over five orders of magnitude in intensity is obtained. Due to the fact that for a mass fractal the exponent directly yields the fractal dimension one can directly deduce that an exponent larger than 3 corresponds to a surface fractal structure. Here the exponent α of the power law is given by $\alpha = 6 - D_s$. Therefore a surface fractal dimension $D_s = 2.26 \pm 0.05$ is immediately obtained.

In evaluating the second moment of the data, the so called invariant J, we take account of the fact that the scattering length densities of Al and Al_2O_3 are not independent from each other (each Al sphere is surrounded by a shell of Al_2O_3) and consider a pseudo two-component system consisting of a mean scattering length density of Al and Al_2O_3 and the scattering length density of the pores being zero. The result strongly depends on the averaging procedure that is determined by the ratio of the Al_2O_3 shell thickness to the radius of the nanocrystalline Al sphere.

Since elemental Al does not dissolve hydrogen, all the hydrogen is concentrated in the amorphous Al_2O_3 layer. From the chemical formula of Section 3.3, $Al/Al_{2.04}O_{3.0}H_{1.11}$, and with the densities $\rho(Al) = 2.70\ g\,cm^{-3}$ and $\rho(Al_2O_3) = 3.4\ g\,cm^{-3}$, respectively,

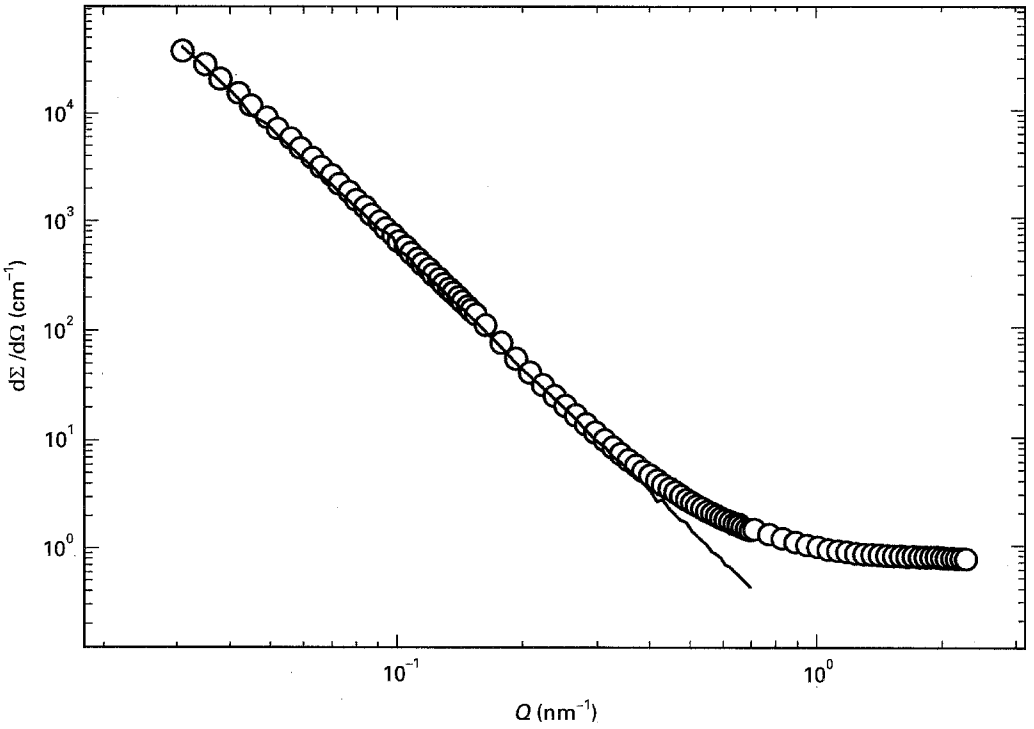

Figure 10 Macroscopic cross-section as a function of scattering vector Q obtained from the SANS experiment. The solid line represents the fit with the model function K_{nm} for independently scattering fractals.

we obtain scattering length densities of 2.08×10^{10} cm^{-2} and 3.70×10^{10} cm^{-2}, and the average scattering length density amounts to 2.9×10^{10} cm^{-2}.

This corresponds to $\Delta\rho$ in Equation 6 since the pores have zero scattering length density. In this way we obtain from the invariant J a volume fraction of scattering centres of $v_c = 0.87$.

Evaluating the incoherent cross-section a value of $d\Sigma/d\Omega_{inc} = 0.85$ cm^{-1} is obtained from the scattering data. If we attribute this completely to hydrogen, we would get a hydrogen particle density of $N/V = 1.34 \times 10^{23}$ cm^{-3}. This indicates a large hydrogen content. We estimate that about half of this scattering intensity is due to background effects (electronic noise, neutrons roaming about in the experimental hall and sample induced background). Unfortunately, a background measurement could not be subtracted because of restrictions in beam time.

5.2.2. Data evaluation in the framework of the fractal model

We have performed a least squares fit of the model by Schmidt [23], Equations 10–14 but without the interference term, to our SANS data. We used $n = 10$, i.e. ten "generations" of spheres, because in evaluating our data we found that the fit improved significantly on approaching $n = 10$ from below, whereas for $n > 10$ no further improvement was obtained. The result of the fit is the solid line displayed in Fig. 10. The fit reproduces the data within the experimental error up to $Q \approx 0.4$ nm^{-1}; above this Q value, or below the corresponding length scale $2\pi/Q \approx 15$ nm, respectively, the fractal behaviour can no longer be observed due to the high incoherent background level. The final parameters, resulting from the fit, are:

$$b = 2.1 \pm 0.1$$
$$R = 261 \pm 2\ \text{nm}$$
$$m = 7.26 \pm 0.05$$

From the scale factor b a surface fractal dimension $D_s = \log 5/\log b = 2.18 \pm 0.14$ is evaluated in agreement with the result of the model independent treatment. The values R and m define the distribution function $\varphi_m(a_0)$ shown in Fig. 9. The most probable radius a_0 of the primary spheres of our fractal amounts to about 2 μm. The 10th generation of spheres then corresponds to $a_{10} = a_0/b^{10} \approx 2$ nm. We emphasize that in low quantity, the existence of comparatively large primary spheres is anticipated from the parameters of the postulated distribution function, although SANS is not sensitive to particles of this large size.

6. Discussion of the microstructure

From the inspection of the electron micrographs, Figs 4–7, it is immediately and directly evident that our composite material consists of spherical particles. Therefore it appears very reasonable to use the single particle form factor of spheres, Equation 12, in the theoretical description of the SANS data. The spheres themselves (this is also directly evident from the micrographs) are again composed of smaller spheres. This already indicates self-similarity and hence fractal behaviour. As an experimental proof of the fractal microstructure we consider the slope of -3.74 of the SANS data in the double-logarithmic plot of Fig. 10 extending over five orders in magnitude in intensity. The value of the slope characterizes our composite as

a surface fractal with a surface fractal dimension of $D_s = 2.26 \pm 0.05$; this dimension is between the value for a truly two-dimensional smooth surface and an extremely fissured "surface", i.e. an essentially three-dimensional body, but closer to the dimension of the surface. Thus we are dealing with a moderately fissured surface.

At Q values above 0.8 nm^{-1} the scattering is dominated by incoherent scattering due to the large hydrogen content of the sample. For that reason we cannot make a statement about the validity of the $Q^{-3.74}$ behaviour beyond Q values of 0.8 nm^{-1}; correspondingly, self-similarity extends at least down to particle diameters of $2\pi/Q \approx 8$ nm. A statement about the upper limit of the length scale of self-similarity is not possible either, because of the $Q^{-3.74}$ behaviour extends down to the lowest Q value of our experiment, 0.03 nm^{-1}, which corresponds to particle diameters of about 210 nm. Thus self-similarity in our composite exists, at least, at particle diameters between 8 and 210 nm.

Although the composite consists of two different chemical phases, we do not consider the different scattering length densities as being the origin of the scattering contrast since the volume fraction of the Al kernel and the Al_2O_3 shells differs from sphere to sphere in a non-coherent way. With an averaged scattering length density inserted into the expression of the invariant J we obtain a volume fraction of scattering centres of 0.87 which corresponds to a porosity of 13%, a reasonable value for a dense packing of differently sized spheres. The large spheres contain large kernels of Al, and this is in full accordance with the observation of sharp Bragg reflections in the X-ray diffractogram. The small Al kernels of the small spheres would result in a broadening of the Bragg reflections but the volume fraction of these small Al kernels is rather small. The Al_2O_3 shell, on the other hand, could not be detected in the X-ray diffractograms which can be due to their noncrystallinity and their small thickness: both effects lead to very broad features in the diffractograms.

For the purpose of a quantitative evaluation of the fractal microstructure (which in a more qualitative way is directly evident from the electron micrographs) we describe our system by the model displayed in Fig. 8, i.e. by spheres which (for reasons of simplicity) in an ordered way are covered by smaller spheres. In our view this model comprises the essential features of the microstructure. In the framework of this model we obtain as quantitative results the average size ratio of spheres of two consecutive generations, $b = 2.1$, and the size distribution of the primary (largest) spheres as shown in Fig. 9. According to this distribution most of the primary spheres have radii between 1 and 3 μm, in full accordance with the micrographs of, for instance, Fig. 4. Also the above mentioned size ratio, $b \approx 2$, can qualitatively be recognized on the micrographs.

In summary, the nanostructured $Al/Al_2O_3(H)$-composite, prepared by a new MOCVD method, has been characterized as a surface fractal; the more qualitative information from the micrographs and the quantitative data from the small angle neutron scattering are complementary to each other; together they yield a rather detailed determination of the microstructure of this new nanostructured material.

Acknowledgements

We thank D. Schwahn (Forschungszentrum Jülich) for fruitful discussions and R. Kampmann (GKSS Geesthacht) for the opportunity to perform the measurements at the SANS facility in Geesthacht. Financial support from the Deutsche Forschungsgemeinschaft in the framework of the SFB 277 is gratefully acknowledged. M. Veith and S. Faber thank the BASF, Ludwigshafen for depositing a patent for the synthesis and use of $(^tBuO)AlH_2$ at the Deutsche Patentamt, No. 19529241.3.

References

1. P. MATTEAZZI and G. LE CAER, *J. Amer. Ceram. Soc.* **75** (1992) 2749.
2. I. J. TOTH, W. D. BRENTNALL and G. D. MERKE, *J. Metals* **24** (1972) 19.
3. M. K. AGHAJANIAN, M. A. ROCAZELLA, J. T. BURKE and S. D. KECK, *J. Mater. Sci.* **26** (1991) 447.
4. G. JANGG, W. WRUSS and A. STUMREICH, *Ber. Dt. Keram. Ges.* **52** (1975) 367.
5. T. WATARI, K. OHTA, N. OHTA, T. TORIKAI and O. MATSUDA, *J. Ceram. Soc. Jpn.* **100** (1992) 1383.
6. T. WATARI, K. MORI, T. TORIKAI and O. MATSUDA, *J. Amer. Ceram. Soc.* 77 (1994) 2599.
7. A. J. SHERMAN and R. H. TUFFIAS, *Ceram. Eng. Sci. Proc.* **11** (1990) 1500.
8. H. O. PIERSON, "Handbook of Chemical Vapor Deposition (CVD)" (Noyes Publications, Park Ridge, New Jersey, USA, 1992).
9. M. VEITH and S. KNEIP, *J. Mater. Sci. Lett.* **13** (1994) 335.
10. T. KODAS and J. HAMPDEN-SMITH, "The Chemistry of Metal CVD" (VCH, Weinheim, New York, 1994).
11. H. C. BROWN and R. F. McFARLIN, *J. Amer. Chem. Soc.* **80** (1958) 5372.
12. ROOKSBY, "X-ray Identification and Crystal Structure of Clay", Joint Committee on Powder Diffraction Standards, JCPDS (1951) p. 264.
13. E. R. ANDREW and W. S. HINSHAW, *R.S.T. Phys. Lett.* **46A** (1973) 57.
14. G POROD, in "Small Angle X-ray Scattering", edited by O. Glatter and O. Kratky (Academic Press, New York, 1982).
15. B. B. MANDELBROT, "Die fraktale Geometrie der Natur" (Birkhäuser, Basel, 1987).
16. P. L. HALL, D. F R. MILDNER and R. L. BORST, *J. Geophys. Res.* **91 B2** (1986) 2183.
17. D. F. R. MILDNER, R. REZWANI, P. L. HALL and R. L. BORST, *Appl. Phys. Lett.* **48** (1986) 1314.
18. H. D. BALE and P. W. SCHMIDT, *Phys. Rev. Lett.* **53** (1984) 596.
19. O. G. POROD, *Kolloid-Z.* **124** (1951) 83.
20. *Idem, ibid.* **125** (1952) 109.
21. P. DEBYE, H. R. ANDERSON and H. BRUMBERGER, *J. Appl. Phys.* **28** (1957) 679.
22. P. WONG, J. HOWARD and J. S. LIN, *Phys. Rev. Lett.* **57** (1986) 637.
23. D. W. SCHÄFER and K. D. KEEFER, *ibid.* **56** (1986) 2199.
24. P. W. SCHMIDT, *J. Appl. Cryst.* **24** (1991) 414.
25. M. HOFFMANN, H. KRÖMER and R. KUHN, "Polymeranalytik I" (Thieme, Stuttgart, 1977).

Received 9 May
and accepted 19 September 1995